Electric Field in a Rectangular Channel with an Electrohydrodynamic Gas Pump

J. Zhang and F. C. Lai
School of Aerospace and Mechanical Engineering
University of Oklahoma
phone: (1) 405-325-1748
e-mail: flai@ou.edu

***Abstract*—Earlier studies have shown that electric field in the form of corona wind can significantly enhance heat and mass transfer. It has also been shown that the maximal enhancement can be achieved by optimal design and arrangement of electrode(s) involved. To this end, a new electrode has been proposed. To seek the optimal design of the electrode as well as the optimal operating conditions, a numerical study has been undertaken. As the first step, electric field generated from the electrode assembly is calculated and verified. The numerical solutions of the three dimensional electrical fields, which are obtained through iterations between the reduced Maxwell equation and the current continuity equation, are presented for some selected operating conditions. Once the electric field results become available, further numerical study on the flow and temperature fields can be continued.**

INTRODUCTION

It has long been known that an electric field can significantly enhance heat and mass transfer [1-3]. In air, the mechanism for this enhancement has been attributed to the electrohydrodynamically (EHD) induced secondary flow. The EHD-induced secondary flow is also known as corona wind or ionic wind, which can be thought of as a micro-jet of fluid issued from the charged electrode to the grounded surface. The net effect of this secondary flow is additional mixing of fluids and destabilization of boundary layer, therefore leading to a substantial increase in the heat and mass transfer coefficients. Corona wind is produced by an electrode charged with a direct current (positive or negative) at a sufficiently high voltage (in the kV range). While the applied voltage may be high, the current involved is usually very small (in the μA to mA range), which makes the power required considerably insignificant. This has become one of the most attractive features for EHD technique.

In recent years, there has been a surge of interest to apply EHD technique to control and manipulate boundary layer separation that leads to drag reduction. Different plasma actuators have been proposed and tested to increase flow attachment to induce more lift on aircrafts [4-6]. Many attempts have also been made to use corona discharge as a driving mechanism for a gas pump [7-8]. More recently, EHD gas pumps were used to drive

gas flow in pipes. These EHD gas pumps are desirable because they are much cheaper to operate since they have no moving part and require less maintenance.

Although EHD gas pumps are promising, there are still some challenging questions to be addressed. The first is associated with the high voltage required to drive the flow in a large scale system. However, it is expected that the operating voltage will decrease as the scale of the system is reduced, thus promoting its wide spread use in microsystems. In fact, the implementation of EHD pumping has received tremendous attention lately due to an increasing interest in microfluidics, chip-integrated cooling, and drug delivery systems [8]. The next challenge is related to its configuration. The efficiency of an EHD pump lies in the design of its electrodes. An appropriate configuration of the pumping system along with an optimal spacing between the electrodes (L) and its relation to other significant dimension (for the present case, the width of the channel; i.e., L/D) must be determined. Finally, the formation of ozone and other ions from the discharge process can lead to health hazards. This concern can limit the applications of EHD pumps if not properly addressed. Not withstanding these minor drawbacks, EHD pumps are attractive for use in the thermal management of electronic and microelectronic circuits since the size of the pump and flow channel can be in the micron or millimeter range.

The main objective of the present study is to numerically evaluate the electric field produced by electrodes used in an EHD gas pump in a rectangular channel. To aid the numerical calculation, experimental measurements have also been conducted. Because of the coupling between electric field and flow fields, the electrical field data obtained from the present study are needed for the further numerical analysis of the flow fields.

EXPERIMENTAL SETUP, NUMERICAL FORMULATION AND PROCEDURE

A. Experimental Setup

The experimental setup used in this study is shown in Fig. 1. The test channel was constructed using Plexiglas of ¼ inch thick. The inner dimensions of the channel were 4 inches by 4 inches with a length of 20 inches. The dimensions of the wire-electrode and system configuration are shown in Fig. 2. A copper wire with a diameter of 20 GA (0.03196 in) was used as the electrode. The copper wire was bent and welded to form the electrode loop as shown. Four one-inch-long copper wires were welded to the base loop at the center on each side of the wall. These four extension wires served as emitting electrodes. A ½ inch wide and 0.025 inch thick copper strip, which was also mounted on all four sides of the wall, was used as the grounded plate. The gap between the tips of the wire and the grounded plate was 1.5 inches. The electrode assembly and the grounded plate were press-fitted to pre-cut grooves on the inner wall of the channel so that their surfaces were flushed with the channel wall. In this arrangement, the corona wind produced by the electrode will resemble that of a wall jet. Also, the emitting electrodes were intended to align with the direction of primary flow to maximize its effect of pumping.

The electrode assembly was connected to a high voltage power supply (Bertan, Series 205B) and charged with a direct current of positive polarity. The plate was grounded

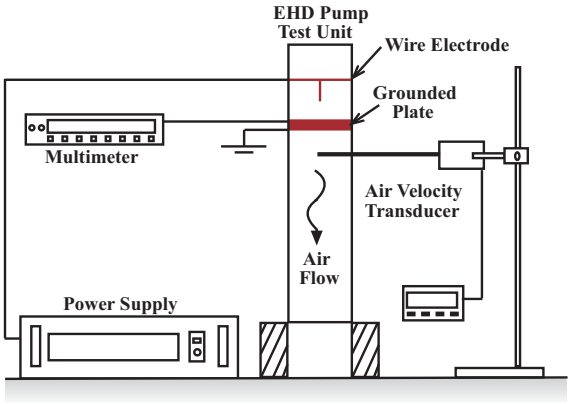

Fig. 1 Schematic of the experimental setup.

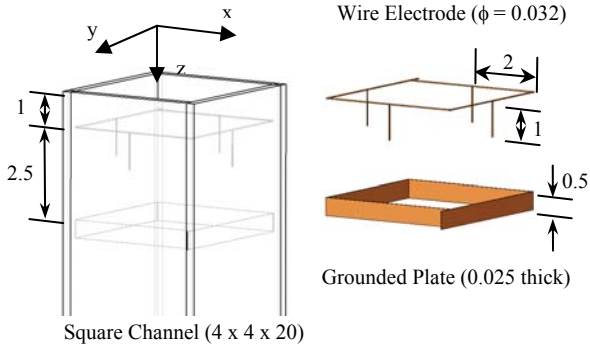

Fig. 2 Configuration of the EHD pump test section with dimensions (in inches).

at the same level of the power supply. A multimeter (Fluke 8000A Series) was connected in series with the ground plate to measure the current flowing through the ground plate.

Two ¼ inch NPT compression fittings were installed on the lower part (outlet section) of the channel to hold the velocity transducer (Omega FMA 902-I) in place to facilitate air flow measurements. The transducer was connected to a process meter (Omega DP 25B-E) so that the measured air velocity can be read out directly. The velocity probe extended horizontally from channel wall allowing measurements along each centerline of the channel cross-section.

Prior to the start of the experiment, a spirit in glass level was used to ensure that the channel was vertically upward and that the velocity probe was horizontally leveled. To avoid electrical shock the power supply was kept in the off position until the start of the experiment. The applied voltage was gradually increased until a flow was detected by the velocity transducer. For the present setup, corona wind was too weak to be detected until the applied voltage was increased to 20 kV. The applied voltage was then incre-

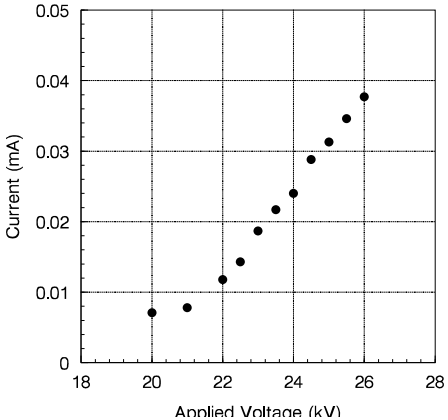

Fig. 3 V-I curve for the present experimental setup.

mentally increased by half kilovolt until spark over occurred at about 25 kV. The phenomenon of sparkover can be easily observed through a visible bright light and cracking sound that it produced. When it occurs, electric field becomes unstable and fluctuates violently. As such, it should be avoided to operate beyond this voltage. The V-I curve for the present experimental setup is shown in Fig. 3. As seen, the current produced by corona discharges increases almost linearly with the applied voltage after the onset of corona.

B. Numerical Formulation and Procedure

For the problem considered, the governing equations for the electrical field are given by [9],

$$\frac{\partial^2 V}{\partial x^2}+\frac{\partial^2 V}{\partial y^2}+\frac{\partial^2 V}{\partial z^2}=-\frac{\rho_c}{\varepsilon}, \tag{1}$$

$$\frac{\partial \rho_c}{\partial x}\frac{\partial V}{\partial x}+\frac{\partial \rho_c}{\partial y}\frac{\partial V}{\partial y}+\frac{\partial \rho_c}{\partial z}\frac{\partial V}{\partial z}=\frac{\rho_c^2}{\varepsilon}, \tag{2}$$

which can be derived from Maxwell equation, current continuity equation and Ohm's law.

The corresponding boundary conditions are,

At the wire, $V = V_0$, (3a)

At the ground plate, $V = 0$, (3b)

At the inlet and outlet of the channel, $\frac{\partial V}{\partial z} = 0$, (3c)

At the left and right channel walls, $\frac{\partial V}{\partial x} = 0$, (3d)

At the front and back channel walls. $\frac{\partial V}{\partial y} = 0$. (3e)

For the solution of electric field, a numerical procedure proposed by Yamamoto and Velkoff [9] has been employed. In this procedure, electric potential and space charge density are determined by iterations on Eqs. (1) and (2) with an assumed value of space charge density at the wire (ρ_{c0}). The validity of the solution is checked by comparing the predicted total current with the measured current at the corresponding voltage. If the currents do not match, a new value of space charge density at the wire is assumed and the calculations are repeated. The flow chart of this algorithm is shown in Fig. 4. There are other algorithms for the solution of electric field (e.g., those proposed by McDonald et al. [10] as well as Kalio and Stock [11]), in which the electrical field condition at the wire is estimated by the Peek's semi-empirical formula [12] instead of an assumed value. It should be pointed out that an empirical constant, named the wire condition factor, has been introduced in the formula mentioned above such that the accuracy of the converged solution really depends on the value of the wire condition factor assigned. Since the assignment of this empirical constant is somewhat arbitrary, we prefer the approach porposed by Yamamoto and Velkoff [9] over the later ones [10-11]. However, it has been reported [13-14] that the agreement between the results obtained by these two approaches is very good when the solutions converged.

Finite different method was used to solve above differential equations along with the boundary conditions. Owing to the symmetry of the problem, only one quarter of the channel was needed for computations. Since the radius of the electrode wire is very small, it is appropriate to treat the wire as a nodal point. A uniform grid (51 x 51 x 176) has been used for the present calculations. As shown in Fig. 4, Eq. (1) is solved first

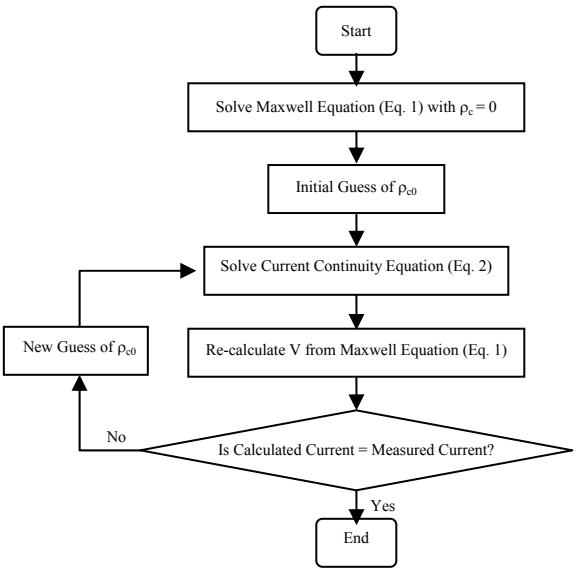

Fig. 4 Flow chart of numerical procedure.

without considering the charge density. The results obtained are used as the initial values of the potential field in the solution for the charge density using Eq. (2). Once the charge density is known, the current on the ground surface can be calculated using the following equation.

$$I_{cal} = \int_0^W \int_0^L \rho_c b E_x \, dydz + \int_0^W \int_0^L \rho_c b E_y \, dxdz, \tag{4}$$

When this calculated current agrees well with the experimental data (i.e., to satisfy Eq. (5)), the electric field is considered converged.

$$\left| \frac{I_{cal} - I_{exp}}{I_{cal}} \right| \le 10^{-3} . \tag{5}$$

Computations have been performed on a 64-bit workstation with 2 GHz CPU and 8 Gb RAM. A typical run takes about one hour of CPU time with 45 minutes for the solution of electric field without charge density and additional 15 minutes for the electric field solution with charge density. A further refinement of grid to 81 x 81 x 256 does not produce much improvement over the results but significantly increase the computational time. As such, the present study settles on the grid of 51 x 51 x 176.

RESULTS AND DISCUSSION

The electric potential distributions inside the test channel are shown in Figs. 5 and 6 without and with the space charge, respectively. The potentials displayed have been normalized with the voltage applied at the wire. The first set of potential contours is viewed from the center planes inside the channel while the second set is viewed from outside of the channel. From Fig. 5, a large potential gradient is observed between the wire electrode and the grounded plate. The electric potential then gradually decreases toward two ends of the channel. By comparing the upper and lower frames of the contours, one observes that the electric potential is slightly higher in the core region of the channel than that on the channel surface. With an increase in the applied voltage, the potential distribution extends further to the two ends of the channel. With the inclusion of space changes, the potential distribution is greatly modified which can be clearly observed from Fig. 6. The potential contour becomes sharpened, particularly at the region close to the electrode. Also, electric potential is extended further toward the ends of the channel.

To better visualize the electric field in three dimensional space, the distributions of electric potential are displayed in various cross-sections in X-Y plane (Fig. 7). For a given applied voltage, one observes that electric potential decreases as one moves along the z-axis toward the outlet. At a given cross-section, the electric field intensifies as the applied voltage increases. For cross-sections at or below the grounded plate, one notices that electric potential is higher at the center of the channel than that at the wall.

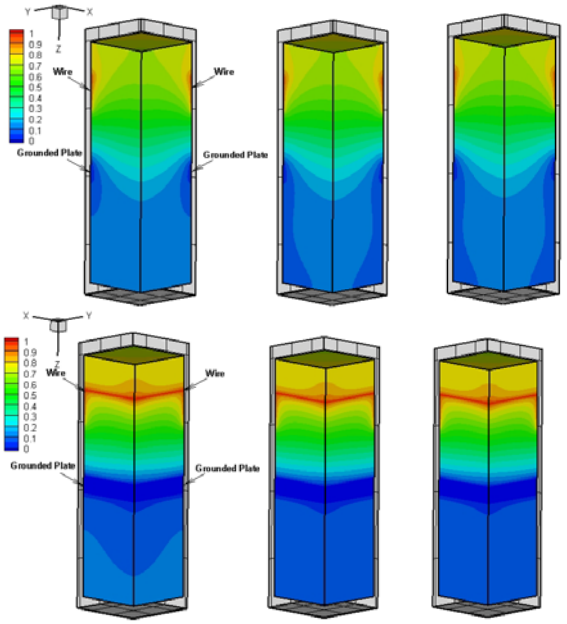

(a) (b) (c)

Fig. 5 Potential distribution in the channel without space charge ($\Delta\bar{v} = 0.05$) , (a) 20 kV, (b) 22.5 kV, (c) 24 kV.

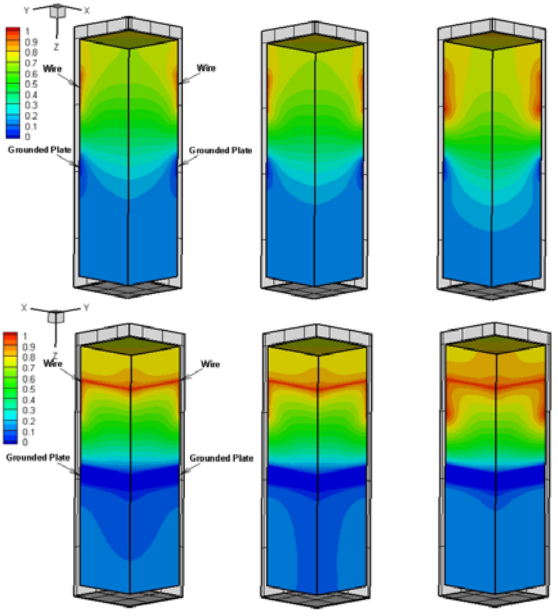

(a) (b) (c)

Fig. 6 Potential distribution in the test channel with space charge ($\Delta\bar{v} = 0.05$): (a) 20 kV, (b) 22.5 kV, (c) 24 kV.

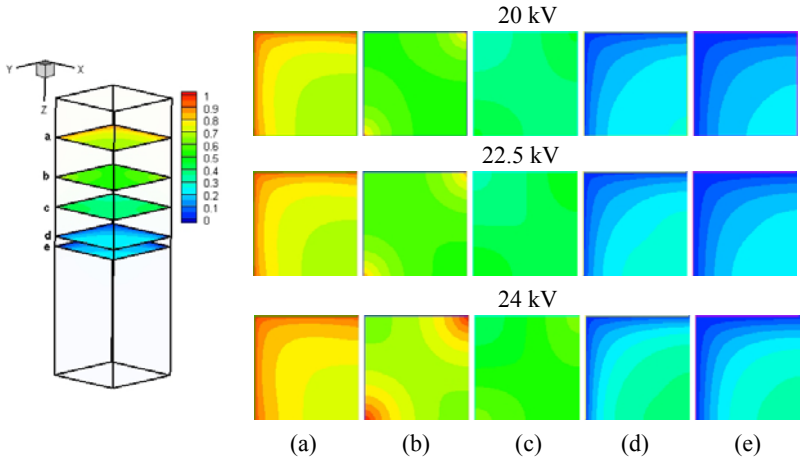

Fig. 7 Potential distribution in X-Y plane ($\Delta\bar{v} = 0.05$): (a) Z = 25.4 mm (the wire plane); (b) Z = 50.8 mm (the wire tip); (c) Z = 69.85 mm (the mid-plane between the wire tip and the grounded plate); (d) Z = 88.9 mm (at the edge of the grounded plate); (e) Z = 95.25 mm (the mid-section of the grounded plate).

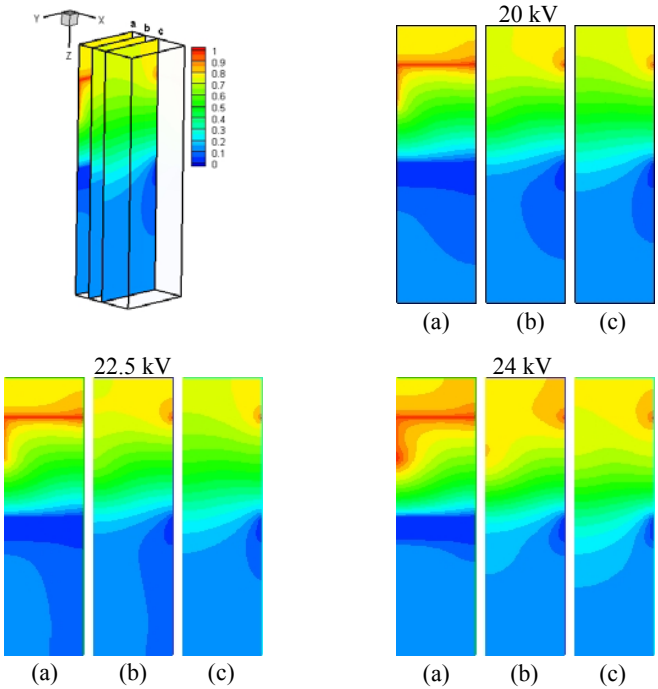

Fig. 8 Potential distribution in Y-Z plane ($\Delta\bar{v} = 0.05$): (a) X = 0 mm (channel wall); (b) X = 12.7 mm; (c) X = 25.4 mm.

The electric field inside the channel can also be examined through the distributions of electric potential in various cross-sections in Y-Z plane (Fig. 8). For a given applied voltage, one observes that a large potential gradient exists at the wire tip and at the edge of the ground plate. The gradient becomes less pronounced as one moves away from the channel wall. Also at a given cross-section, the electric field intensifies as the applied voltage increases.

The distributions of space charge are shown in Fig. 9 for various potentials considered. The charge density displayed is also normalized with its value at the wire tip. As observed, space charges are clustered around the wire tip. Their density reduces significantly when moving away from the wire tip. With an increase in the applied voltage, the cluster of space charges is further confined to a smaller region at the tip.

To visualize the charge distribution in three dimensional space, the distributions of space charge are displayed in various cross-sections in X-Y plane as well (Fig. 10). For a given applied voltage, one observes that there is no space charge on the wire plane above the tip since space charge propagates like a one-dimensional wave toward the grounded plate. As one moves along the z-axis toward the grounded plate, space charge gradually spreads from the wire tip to the center of the channel. With an increase in the applied voltage, space charge spreads wider. At a given cross-section, space charge is observed to spread radially outward from the wire tip. For cross-sections at the grounded plate level, one notices that the distribution of space charge is nearly uniform.

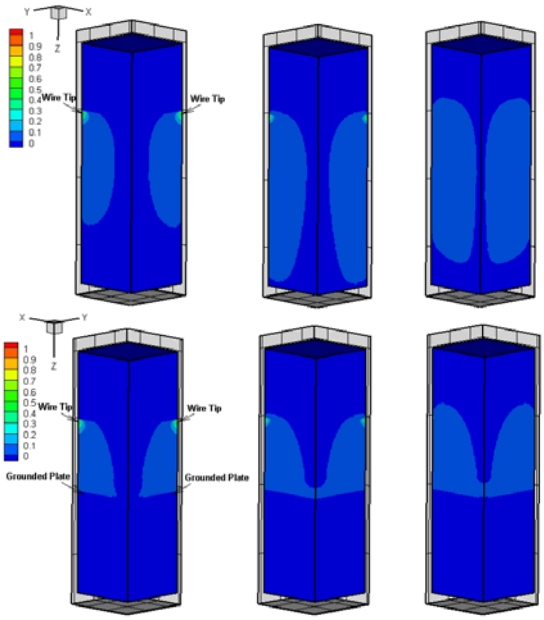

Fig. 9 Space charge distribution in the test channel ($\Delta \overline{\rho_c} = 0.1$): (a) 20 kV, (b) 22.5 kV, (c) 24 kV.

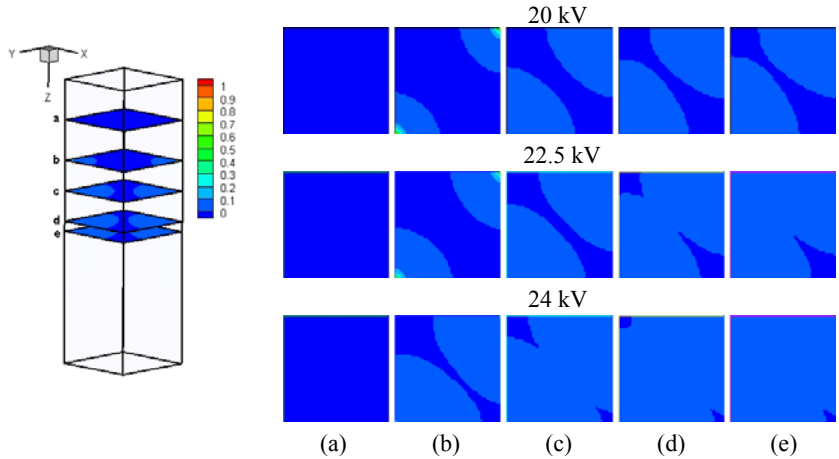

Fig. 10 Space charge distribution in X-Y plane ($\Delta\overline{\rho_c}$ = 0.1): (a) Z = 25.4 mm (the wire plane); (b) Z = 50.8 mm (the wire tip); (c) Z = 69.85 mm (the mid-plane between the wire tip and the grounded plate); (d) Z = 88.9 mm (at the edge of the grounded plate); (e) Z = 95.25 mm (the mid-section of the grounded plate).

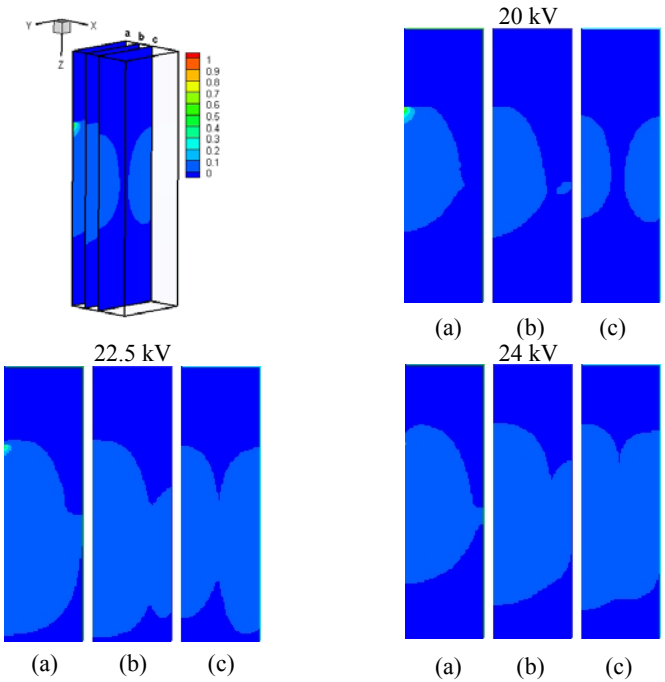

Fig. 11 Space charge distribution in Y-Z plane ($\Delta\overline{\rho_c}$ = 0.1): (a) X = 0 mm (channel wall); (b) X = 12.7 mm; (c) X = 25.4 mm.

The spread of space charge in the longitudinal direction can be examined from the contour plots in Y-Z plane (Fig. 11). At the wall, it is observed that space charge spreads from the wire tip toward the channel outlet. As one moves away from the wall, the influence from the other wire tip becomes obvious. From Figs 10 and 11, one concludes that space charge although weak distributes rather uniform in the core region of the channel.

CONCLUSION

The present study examines the electric field inside a rectangular channel equipped with an EHD gas pump. From the numerical results obtained, one can visually inspect the distribution of potential and space charge. The results obtained provide the needed information for further numerical analysis of flow field. Through the study of coupled flow field, one will be able to optimize the design of an EHD gas pump.

NOMENCLATURE

b	ion mobility of air, b = 1.4311 x 10^{-4} $m^2/V{\cdot}s$ for positive ions
E_x	electric field strength in x-direction
E_y	electric field strength in y-direction
I_{cal}	numerically calculated corona current
I_{exp}	experimentally measured corona current
L	length of channel
V	electric potential
V_0	applied voltage at the wire
$\overline{V}$	normalized electric potential, = V/V_0
W	width of channel
x, y, z	Cartesian coordinates
ε	permitivity of air
ρ_c	space charge
ρ_{c0}	space charge at the wire tip
$\overline{\rho_c}$	normalized space charge, = ρ_c/ρ_{c0}

REFERENCES

[1] T. B. Jones, Electrohydrodynamically Enhanced Heat Transfer in Liquids – A Review, *Advances in Heat Transfer*, vol. 14, pp. 107-148, Academic Press, New York, 1978.

[2] J. H. Davidson, F. A. Kulacki and P. F. Dunn, Convective Heat Transfer with Electric and Magnetic Fields, *Handbook of Single-Phase Convective Heat Transfer*, edited by Kakac, S., et al., Wiley, New York, 1987.

[3] J. Seyed-Yagoobi and J. E. Bryan, Enhancement of Heat Transfer and Mass Transport in Single-Phase and Two-Phase Flows with Electrohydrodynamics, *Advances in Heat Transfer*, vol. 33, pp. 95-186, 1999.

[4] M. L. Post and T. C. Corke, "Separation Control on High Angle of Attack Airfoil Using Plasma Actuators," *AIAA Journal*, vol. 42, pp. 2177-2184, 2004.

[5] C. L. Enloe, T. E. McLaughlin, R. van Dyken, K. D. Kachner, E. J. Jumper and T. C. Corke, "Mechanisms and Responses of a Single Dielectric Barrier Plasma Actuator: Plasma Morphology," *AIAA Journal*, vol. 42, pp. 589-594, 2004.

[6] C. L. Enloe, T. E. McLaughlin, R. van Dyken, K. D. Kachner, E. J. Jumper, T. C. Corke, M. L. Post and O. Haddad, "Mechanisms and Responses of a Single Dielectric Barrier Plasma Actuator: Geometric Effect," *AIAA Journal*, vol. 42, pp. 595-604, 2004.

[7] J. Seyed-Yagoobi, "Electrohydrodynamic Pumping of Dielectric Liquids," *Journal of Electrostatics*, vol. 63, pp. 861-869, 2005.
[8] D. J. Laser and J. G. Santiago, "A Review of Micropumps," *Journal of Micromechanics and Mircoengineering*, vol. 14, pp. R35-R64, 2004.
[9] T. Yamamoto and H. R. Velkoff, "Electrohydrodynamics in an Electrostatic Precipitator," *Journal of Fluid Mechanics*, vol. 108, pp. 1-18, 1981.
[10] J. R. McDonald, W. B. Smith, H. W. Spencer and L. E. Sparks, "A Mathematical Model for Calculating Electrical Conditions in Wire-Duct Electrostatic Precipitation Devices," *Journal of Applied Physics*, vol. 48, pp. 2231-2243, 1977.
[11] G. A. Kallio and D. E. Stock, "Computation of Electrical Conditions Inside Wire-Duct Electrostatic Precipitators Using a Combined Finite-Element, Finite-Difference Technique," *Journal of Applied Physics*, vol. 59, pp. 999-1005, 1985.
[12] F. W. Peek, *Dielectric Phenomenon in High Voltage Engineering*, McGraw-Hill, New York, 1966.
[13] F. C. Lai, P. J.Mckinney and J. H. Davidson, "Oscillatory Electrohydrodynamic Gas Flows," *Journal of Fluids Engineering*, vol. 117, pp. 491-497, 1995.
[14] F. C. Lai and S. S. Kulkarni, "Effects of Buoyancy on EHD-Enhanced Forced Convection in a Vertical Channel," *Journal of Thermophysics and Heat Transfer*, vol. 21, pp. 730-735, 2007.